RSC Advances

ROYAL SOCIETY OF CHEMISTRY

www.rsc.org/advances

Glucose Detection Using SERS with Multi-branched Gold Nanostructures in Aqueous Medium

Andrea Ceja-Fdez[a], Tzarara López-Luke[a]*, Alejandro Torres-Castro[b], Damon. A. Wheeler[c], Jin Z. Zhang[d] and Elder De la Rosa[a]*

[a]Centro de Investigaciones en Óptica, A.P. 1-948, León, Gto. 37150, México.
[b]Universidad Autónoma de Nuevo León, CIDIIT-FIME, UANL, San Nicolas de los Garza, Nuevo León C.P. 66451, México.
[c]Department of Chemistry and Chemical Biology, University of California, Merced, CA 95343, USA
[d]Department of Chemistry and Biochemistry, University of California, Santa Cruz, CA 95064, USA

Corresponding author: elder@cio.mx* and tzarara@cio.mx*

Abstract. Gold nanoparticles (AuNPs), multi-branched gold nanoparticles (MBGNs), and silica-coated MBGNs (MBGNs-silica) were studied for Rhodamine B (RB) and α-glucose detection at low concentration. The MBGNs SPR band in the NIR, which is tunable, is useful for SERS that was demonstrated using Rhodamine B and α-glucose as probe molecules with detection limits of 50 pM and 5 mM (90 mg/dL), respectively, much lower than that using regular AuNPs. The SERS signals of RB and α-glucose using MBGNs-silica are further enhanced with respect to AuNPs and MBGNs, which is attributed to the aggregation of the MBGNs and a stronger interaction. In the case of α-glucose, the functionalization process performed to both, α-glucose molecules and MBGNs, improves the interaction and allows measurements at low concentration.

Keywords: SERS, Glucose, Gold Nanostructure and multi-branched gold

1. Introduction

The detection of molecules at low concentration in solution with high sensitivity and specificity has been of great interest in fields such as biomedical research and diagnosis [1-

4]. In particular, surface-enhanced Raman scattering (SERS) is a powerful, ultrasensitive, and non-destructive spectroscopic technique that can detect analytes down to the single molecule level while simultaneously providing molecular specific information [5-7]. Many studies have demonstrated enhancement factors of 10^5 or higher, leading to Raman signals that are comparable to or even higher than those of the fluorescent organic dyes [8-10]. SERS is a technique resulting in strongly increased Raman signals of molecules at or near metal nanostructures, typically noble metals such as gold and silver. In particular, SERS has been exploited to detect low concentration of biological samples such as different types of cancers [11-16], Alzheimer's disease (β-amyloid peptide) [17,18], the hepatitis C virus [19], and Parkinson's disease (dopamine depletion) [20,21]. In the study of SERS processes, it is generally accepted that electromagnetic enhancement [22] and chemical enhancement [23] mechanisms are the principal phenomena involved in the amplification of Raman signals. Effective SERS depends on absorption of incident light by the metal nanostructures based on their surface plasmon resonance (SPR) [22] where the excitation wavelength is resonant with the metal-molecule charge transfer electronic states [23]. The success of SERS is highly dependent on the interaction between adsorbed molecules and the surface of plasmonic nanostructures. In the last years, many studies have strived to optimize substrate structure and configuration to maximize enhancement factors such as new plasmonic materials [24-26] with different shapes and sizes [27,28] that support increased SERS enhancement. The SPR of a metal nanoparticle may be tuned throughout visible and near-infrared (NIR) wavelengths by varying the size and shape or the aspect ratio [29-32]. Particularly, the plasmons of metallic nanostars, nanoshells, and nanorods can be used to tune the SPR into the NIR region [33-39], which is desired for *in vivo* biomedical applications due to deeper tissue penetration [40-42].

Gold nanoparticles have been widely studied for bio detection applications due to their unique optoelectronic properties. Various types of AuNPs [43-46], both in aqueous [47-49] and organic solutions [50,51], have been developed to serve as excellent SERS substrates. Moreover, the silanization of various metal nanoparticle systems has shown great success in protecting their surface characteristics and facilitating bioconjugation [52,53]. The SERS activity of gold and silver nanostructures has been experimentally verified using

Rhodamine B as an analyte due to its distinct Raman features and adsorbability onto nanoparticles [54,55].

One of the important applications of SERS is detection of glucose. Glucose in particular is interesting as proper monitoring of diabetes mellitus requires effective screening of glucose levels within human blood. Several studies have been reported previously [56-59]. Van Duyne and coworkers have done extensive work on SERS detection of glucose [60-62] in which they observed that SERS was successful in the detection of glucose at physiological concentrations using *in vitro* and *in vivo* sensing techniques. Yang and coworkers proposed the use of a photonic crystal fiber as a container of a different concentration solutions of D-glucose, and obtained a low concentration detection *via* Raman spectroscopy [63]. Dinish *et al*. implemented a nanogap SERS substrate with a deep-UV lithography technique for glucose sensing [64]. Very recently, Al-Ogaidi worked with gold nanostar@silica core–shell nanoparticles conjugated with glucose oxidase (GOx) enzyme molecules developed as the SERS biosensor for label-free detection of glucose, by examining SERS peak of H_2O_2 [65]. However, it is still challenging to achieve high reproducibility, good uniformity, and long-term stability of SERS substrates. As mentioned, glucose is extremely difficult to detect through conventional SERS methodologies because of its small Raman cross-section and weak absorption to bare metal surfaces.

In the present work, we have carried out a systematic study of the SERS signals of Rhodamine B (RB) and α-glucose adsorbed on colloidal multi-branched gold nanostructures (MBGNs) and MBGNs with a silica coating. The MBGNs demonstrated their ability to detect these two molecules at low concentrations, compared to AuNPs where no Raman signal was observed. While MBGNs serve to enhance the Raman signal, the MBGNs-silica coating induce aggregation and then affords strong interaction with RB and α-glucose resulting in an increase of hot spot density that improve the SERS signal. Since SERS detection of α-glucose in water is generally challenging, the successful detection within a clinically relevant concentration range shows the promise of the MBGNs and MBGNs-silica as potential SERS substrates for detecting molecules that strongly interact with silica coating or MBGN surface itself.

2. Experimental

2.1 Materials.

All chemicals were reagent grade. $HAuCl_4$, sodium citrate, silver nitrate, ascorbic acid, 3-aminopropyltriethoxysilane (APTES), Rhodamine B and α-glucose were purchased from Sigma-Aldrich. HCl was purchased from Karal, (~38% in H_2O), deionized water was purchased from Quimicurt, and ethanol was purchased from Jalmek.

2.2 Preparation of MBGNs and MBGNs-silica

Multi-branched gold nanostructure (MBGNs) were prepared by a seed-mediated growth method following previously reported protocols with some modifications [66] where a gold seed solution was synthesized using the Turkevich method [49]. Briefly, the addition of a 1% citrate solution to a boiling solution of 1 mM $HAuCl_4$ under stirring yielded a red color characteristic of gold nanospheres (AuNP). The stable particles were filtered by Whatman filter papers of 110 nm, and then kept at 4 °C for long-term storage. To synthesize MBGNs, 200 µl of the previously prepared seed solution was added to 10 ml of 0.5 mM $HAuCl_4$ solution with 40 µl of 1M HCl at room temperature under moderate stirring. Quickly, 40 µl of 0.01M silver nitrate and 126 µl of 0.1 M ascorbic acid were added simultaneously under 700 rpm stirring. It is believed that the major role of Ag^+ is to assist the anisotropic growth of Au branches on certain crystallographic facets on multi-twinned citrate seeds [67-70]. The color rapidly turned from light red to greenish-black, indicating the formation of MBGNs. MBGNs-silica were prepared by adding 10 µl of 10% vol. APTES solution to the MBGNs solution that had been previously prepared.

2.3 AuNPs and MBGNs linked with Rhodamine B and α-glucose.

High concentration of RB aqueous solution (1x10-2M) was prepared to obtain the characteristic Raman spectra of concentrated RB. RB-MBGNs solutions were prepared by dissolving solid RB in distilled water and three different concentrations were obtained (1x10-7 M, 1x10-8 M and 1x10-10 M), then 500 µl of these RB solutions were mixed with

500 µl of colloidal MBGNs having RB-MBGNs final concentrations of 0.5x10-7 M, 0.5x10-8 M and 0.5x10-10 M respectively. Furthermore, RB-MBGNs-Silica was prepared as follows: first was prepared RB-APTES solutions adding 10 µl of 10 %vol. APTES solution to the three concentrations of RB solutions (1x10-7 M, 1x10-8 M and 1x10-10 M). Subsequently 500 µl of colloidal MBGNs-silica, were added to 500 µl of each RB-APTES concentrations. And finally 500 µl of colloidal AuNPs and AuNPs-APTES were added to a 500 µl of the highest concentrated simple (1x10-7M) RB and RB-APTES solutions, to obtain RB-AuNPs and RB-AuNPs-silica respectively.

A sample of high concentration of α-glucose was prepared by dissolving 50 wt% of α-glucose in water. Additionally, α-glucose-MBGNs solutions were prepared by dissolving solid α-glucose in 100 µl of distilled water and mixed with 900 µl of colloidal MBGNs obtaining final concentrations of 5 mM, 10 mM and 20 mM (90, 180 and 360 mg/dL) respectively. The α-glucose-MBGNs-silica was prepared by dissolving solid α-glucose in 100 µl of distilled water and adding 10 µl of 10%vol. APTES solution and mixed with 900 µl of colloidal MBGNs-silica (5 mM, 10 mM and 20 mM respectively). And α-glucose-AuNPs-silica was prepared adding 900 µl of colloidal AuNPs (with and without APTES) to a 100 µl of α-glucose and α-glucose-APTES solutions obtaining a 20mM concentration, respectively.

2.4 Morphology and optical characterization.

The morphology and size of the AuNPs and MGBNs-silica were analyzed by transmission electron microscopy (TEM) using a FEI Titan 800-300 with accelerating voltage set to 300 kV. UV-Vis absorption measurements were carried out using a Perkin Elmer Lamda 900 spectrometer with a spectral resolution of 2 nm. Raman spectra were collected using a Renishaw Raman System (inVia Raman Microscope) with a 20× objective lens and the excitation laser was operated at 785 nm. The integration time for each Raman measurement was 20 s. For the Raman signal detection, the laser excitation light was directly focused onto the surface of the sample solution (250 µl) with a laser power of ~5mW and the aforementioned integration time.

2.5 Zeta Potential

Zeta potential measurements were carried out using a Malvern Instrument Zetasizer Nano (red laser 633 nm) to the following samples, α-glucose in water (100 mM), α-glucose-APTES (100 mM), colloidal MBGNSs and colloidal MBGNs-silica. The samples were dispersed in distilled water (1 mM, pH = 7.4) with a concentration of 1 mg/mL

3. Results

The size and morphological characterizations were performed by TEM images, and are shown in Figure 1(a)-(d), where it was confirmed that AuNPs were obtained with an overall outer diameter of ~20 nm, see Figure 1(a)-(b). These AuNPs were mixed with silver nitrate at a 2:1 volume ratio and used as seeds to synthetize the MBGNs with an average size of 200 nm, as is shown in Figure 1(c)-(d). It is observed that the MBGNs are surrounded by a cloud of silica that promotes the agglomeration, having MBGNs- silica clusters of ~ 1000 nm, see Figure 1 (d).

Figure 2 shows the UV-Vis Spectrum of (a) AuNP, (b) MBGNs and (c) MBGNs-silica, dispersed in aqueous solution. For AuNP, the SPR is centered at 522 nm, as is shown in Figure 2(a) and for the MBGNs and MBGNs-silica the SPR was red-shifted to 850 nm, see Figure 2 (b)-(c). The absorption spectrum of the MBGNs-silica sample shows a wide band, which is consistent with the agglomeration of the particles, due to the interplay between the silica coating and the underlying MBGNs resonances, about which more will be discussed later. This is consistent with the dimensional results gleaned from the TEM images of Figure 1(a)-(d). These large spectral shifts from the nanospheres are manifested as color changes in the colloidal solutions of the nanoparticles, as is shown in Figure 3. In the image, AuNP are represented by the red solution and the MBGNs-silica solution is the greenish black solution, as seen in Figure 3(a) and (b), respectively. The color changes are not significant between MBGNs and MBGNs-silica solutions.

SERS activity of the AuNPs, MBGNs and MBGNs-Silica was examined using RB as Raman marker. The comparative SERS spectra of varying the concentration of RB, and the effect of APTES addition in AuNP and MBGNs is displayed in Figure 4. The Characteristic Raman signals obtained from a RB high concentrated solution (0.01 M) that

yields peaks at 620, 1195, 1275, 1358, 1431, 1506, 1527, 1591 and 1647 cm^{-1} is displayed in Figure 4(A) and is in agreement with results reported recently [69]. In Figure 4(B) are shown the resulting Raman spectra of using AuNPs with and without silica in RB detection and compared with the AuNP 0M spectra, where the characteristic peaks were not observed even at relative high concentration (1×10^{-7} M), however for AuNPs-silica an small peak at 850 cm^{-1} is observed. The Raman signal of three concentrations of RB (10^{-10}, 10^{-8} and 10^{-7} M) adsorbed on MBGNs and MBGNs-silica are displayed in Figure 4C (b-d) and (e-g), respectively. The Raman signal of RB adsorbed on MBGNs show peaks at 628, 1284, 1364, 1516, 1534 and 1655 cm^{-1}, see Figure 4(C) (b-d) and RB adsorbed on MBGNs-silica at 620, 1196, 1268, 1349, 1452 and 1503 cm^{-1}, see figure 4(C) (e-g). It is observed that band positions present small changes with the presence of the silica coating about which more will be discussed later. Figure 4(D) shows the increase of the Raman signal by using MBGNs and MBGNs-silica with different concentration of RB (10^{-10}, 10^{-8} and 10^{-7} M), each data point represents the average value from three SERS spectra and error bars show the standard deviations. There is a linear relationship between the intensity of the 628, 1284 and 1516 cm^{-1} bands and RB concentration. The silica coating enhanced the Raman signal by ~ 3 times in comparison when using samples without silica coating.

Figure 5 shows SERS spectra of the α-glucose using colloidal AuNPs, AuNPs-silica, MBGNs and MBGNs-silica as the SERS substrates. In Figure 5(A) is presented the spectrum of a high concentration α-glucose in water (50 % wt) and several vibrational peaks were seen at 512, 845, 912, 1033, 1114 and 1333 cm^{-1}. These are the typical bands of α-glucose/water [71]. Figure 5(B) shows the Raman results of testing the detection of α-glucose (20 mM) using AuNPs and AuNPs-silica and compared with the AuNP 0M spectra, where the characteristic Raman signal is not observed, however for AuNPs-silica only an small peak at 850 cm^{-1} is observed. Figure 5(C) displays several SERS spectra taken at varying α-glucose concentrations (0, 5, 10 and 20 mM), showing the potential limit of detection using the MBGNs and MBGNs-silica, see Figure 5(C)(a-d) and (e-g) respectively, where 5(C)(a) corresponds to 0 mM. It is interesting the small yet consistent and reproducible blue-shift of the 512 and 1114 cm^{-1} vibrational bands observed in samples of α-glucose adsorbed in MBGNs-silica. The reason for this small shift will be discussed

later. As expected, they increase in intensity with increasing the α-glucose concentration. This relationship is shown clearly in Figure 5(D), which shows a plot of the integrated signal of the 512, 1033 and 1114 cm^{-1} vibrational bands. A linear relationship between the intensity of the signal and α-glucose concentration was observed. Each data point represents the average value from three SERS spectra and error bars show the standard deviations. It is observed a ~2 times increment of the Raman signal for samples using MBGNs with silica coating compared to uncoated nanoparticles.

Figure 6 shows a schematic diagram for the preparation of α-glucose bonded to silica coated MBGNs. It is schematized the preparation of MBGNs-silica bonded to α-glucose-APTES. First AuNPs were prepared to be used as a seed to obtain the MBGNs with a positive surface charge of +34 mV, the process is explained in the experimental section. After that, APTES was added to the colloidal MBGNs binding through amines groups, obtaining MBGNs-silica (+25 mV), having the OH- groups exposed. On the other hand, α-glucose-APTES was prepared as mentioned in the experimental section. The α-glucose surface charge is -18 mV, increasing negatively for α-glucose-APTES to -46 mV, suggesting OH- in the surface. Therefore we are proposing the binding of α-glucose-APTES to the MBGNs-silica through electrostatic forces and hydroxyl groups bonds.

4. Discussion

To interpret the Raman signal enhancement properties of MBGNs, it is necessary to analyze the structural changes and optical properties of these nanostructures. The Figure 1(a, b) shows the spherical gold nanoparticles (AuNPs) with an overall size of ~20 nm prepared by following the Turkevich method [72]. Such particles were used as seeds that in combination with HCl, silver nitrate, and ascorbic acid promote the anisotropic growth of Au branches on certain crystallographic facets on multi-twinned citrate gold seeds resulting on a multibranched nanoparticle (MBGNs) obtained in the absence of surfactant, see Figure 1(c). As has been reported the presence of Ag^+ ions, and the Cl^- produced during the Au reduction of $HAuCl_4$, precipitate with the Ag^+ ions forming AgCl on the surface of the growing AuNPs. The growth process and the morphology of the final Au product are affected inevitably, so that the AuNPs could not isotropically expand to large gold spheres

but form the MBGNs [73]. Figure 1(d) shows the MBGNs aggregation enveloped by a gray coating of SiO_2, induced by small amount of the addition of APTES.

The SPR of AuNPs situated in 522 nm, was consistent with the particle size and the color of AuNPs solution obtained with the Turkevich method. In the case of MBGNs and MBGNs-silica the SPR is shifted to 850 nm, which is indicative of the MBGNs nature [66]. It is in accordance with the results reported in the literature where the red-shift was produced from the deviations from spherical geometry [74]. This is related with the interaction of electric field of the incoming radiation and the nanoparticle, in which it induces the formation of a dipole in the nanoparticle, and there is a restoring force that tries to compensate it, so that a unique resonance frequency matches this electron oscillation within the nanoparticle. For non-spherical particles, such as rods or branches, the resonance wavelength depends on the orientation of the electric field relative to the particle [75]. The optical properties of non-spherical particles are highly affected due to size variations of anisotropic shapes and this is because the quite differences in frequencies associated with the various resonance modes. These resonances has been modeled *via* Mie for small spheres [76] and their modification by Gans for ellipsoids [77]. As seen in Figure 2(b) and in Figure 2(c), it is observed that the silica coating expand the width in the green region of SPR peak [78,59]. This is most likely due to the polydispersity of ~22% of MBGNs-silica agglomerates and is consistent with the results collected from the TEM images in Figure 1 and with the color changes in figure 3.

As can be seen in figure 4(B) it was difficult to obtain the characteristic Raman signal of RB adsorbed on AuNPs and AuNP-silica, suggesting that the enhancement factor is weak as has been reported for a spherical nanoparticle, but an small peak is observed at 850 cm^{-1} for AuNP-silica, corresponding to Si–OH stretching and bending as has been reported [79]. However, when MBGNs and MBGNs-silica were used, the characteristic Raman signal of RB was clearly observed, see Figure 4(C). Such enhancement of the Raman signal is the result of the electromagnetic field improvement probably produced by the anisotropic structures increasing the density and number of hot spots, especially at the tip of the branches as a result of the nano antenna effect [80]. The three times improvement of the Raman signal observed with the introduction of silica coating is probably due to the

proximity of the MBGNs, inducing the formation of hot spots with greatly enhanced localized electromagnetic field [81,82]. It has been reported that the carboxylic group of RB is conjugated with APTES through a condensation reaction, and yields a silanized RB which was covalently incorporated into silanol groups present on surface modified of gold nanostructures by Si-O-Si bonds [83]. The assembly of MBGNs with silica coating as a reproducible method has been widely applied to SERS studies. Furthermore, improvement of the Raman signal by silica coating is also result of the augmentation of the bandwidth by which resonance with pumping signal is stronger. It is observed that band positions are blue-shifted with the presence of the silica coating in addition to the concomitant increases in the Raman signal. The increment of individual Raman signal peaks (628, 1284 and 1516 cm^{-1}) as a function of RB concentration follow a linear relationship with slopes of 0.5, 2 and 3 for MBGNs respectively and 1, 3 and 5 for MBGNs-silica, respectively, see Figure 4(D). This mean, MBGNs-silica coated is almost twice sensitive than uncoated nanoparticles making possible the detection of analyte concentration as lower as 10^{-10} M of RB, not detected with uncoated nanoparticles. Such result shows the relevance of the coating of MBGNs improving the interaction with analyte and increasing the hot spot.

As in the case of RB, the detection of α-glucose in water (20 mM) by using colloidal AuNPs and AuNP-silica was unsuccessful as displayed in Figure 5(B) and the 850 cm^{-1} peak is due to the presence of Si-OH stretching and bending [79]. However, α-glucose was measured with colloidal MBGNs for concentration as lower as 5 mM. As expected according to results described before on RB, the Raman signal was improved when silica coated MBGNs were used, see Figure 5(C). The agglomeration induced by APTES served to increase SERS signals due to the higher density of SERS hot spots [84]. As shown in figure 5(D), there is a linear relationship between the individual Raman signal peaks (512, 1033 and 1114 cm^{-1}) and α-glucose concentration. The slopes of the linear relationship for uncoated MBGNs is 6, 10 and 10 respectively, and 8, 30 and 20 respectively for silica coated MBGNs. Notice the small blue-shift due to the bonding between the hydroxyl groups of α-glucose-APTES and the free hydroxyl groups of MBGNs-silica particles [85] and through unions by electrostatic forces, as is proposed in Figure 6. Therefore, the functionalization proposed here is an effective way to improve interaction between MBGNs and glucose molecule, resulting on an strong enhancement of the Raman signal. These

results confirm that colloidal MBGNs is an effective tool for measuring clinical concentration of α-glucose, and it is three time more sensitive when such particles are silica coated. The methodology proposed here for α-glucose measurement is simple, very reliable and cheaper because does not require special instrumentation other than Raman spectrometer.

5. Conclusions

In this work, we have demonstrated that MBGNs are highly SERS-active for quantitative RB and α-glucose detection in low concentrations in aqueous media. We compared the Raman enhancement when using MBGNs and MBGNs-silica and the signal is increased by ~250% and ~350%, respectively. Such enhancement is attributed to the increase of hot spot because of the morphology and the strong interaction between the analyte (RB and α-glucose) and MBGNs-silica. The functionalization process performed to both glucose molecules and MBGNs improved such interaction and make possible the measurement of concentration as lower as 5 mM (90 mg/dL). This is very important since α-glucose has been notoriously difficult to detect by SERS due to its small Raman cross-section and weak interaction with bare metal surfaces. We believe this crucial adsorption problem has been overcome due to the chemical interplay between hydroxyls on the silica surface and the α-glucose structure which facilitates the chemical adsorption. The measurement of α-glucose in water is important because mimics well the chemical environment of the human body. Future endeavors will center on the detection of glucose in body fluids like blood, urine or tears.

Figure Captions.

Figure 1. TEM image of AuNPs (a and b) with average size of ~20 nm, which were used to prepare MBGNs (c) with average diameter 200 nm. Aggregates of MBGNs-silica (d) resulting in an average size of 1000 nm.

Figure 2. UV-Vis absorption spectra of (a) AuNPs, (b) MBGNs and (c) MBGNs-silica, dispersed in aqueous solution

Figure 3. Color Comparison of the solutions. (a) AuNPs (red solution), used as a seed for the synthesis of (b) MBGNs-silica (green-black).

Figure 4. (A) Raman spectra obtained from a concentrated solution (0.01 M) of Rhodamine B in distilled water. (B) Raman signal of AuNP 0M and AuNP and AuNP-silica with RB solution at $1x10^{-7}$ M. (C) Representative SERS spectra following 785 nm excitation obtained from: (a) Target MBGNs-silica, and RB at different concentration, $0.5x10^{-10}$, $x10^{-8}$ and $x10^{-7}$ M on MBGNs (b), (c) and (d), and (e-g) for silica coated MBGNs. (D) A plot of the integrated Raman signal for three peaks, (628, 1284 and 1516 cm^{-1}) vs. the RB concentration as RB on MBGNs (RB/MBGNs) and RB-APTES solution on MBGNs-silica (RB/MBGNs-silica). Each point represents the average value from three SERS spectra and error bars show the standard deviations.

Figure 5. (A) Raman spectra obtained from a concentrated solution of α-glucose in distilled water (50% wt.). (B) Raman signal of AuNP 0M and AuNPs and AuNP-silica with α-glucose in water at 20 mM, (C) Representative SERS spectra following 785 nm excitation obtained from: (a) Target MBGNs-silica, and α-glucose at different concentrations (5, 10 and 20 mM) on MBGNs (b-d), and (e-g) for silica coated MBGNs. In this last case, α-glucose was functionalized with APTES. (D) A plot of the integrated Raman signal (512, 1033 and 1114 cm^{-1}) vs. α-glucose concentration as α-glucose on MBGNs (α-glucose/MBGNs) and α-glucose/APTES solution on MBGNs-silica (α-glucose/MBGNs-silica). Each point represents the average value from three SERS spectra and error bars show the standard deviations.

Figure 6. Schematic diagram showing hypothetical addition of α-glucose to MBGNs. APTES solution was added to the MBGNs, and α-glucose/APTES solution was prepared and subsequently both solutions were mixed. This facilitated the α-glucose incorporation through the bonds of hydroxyl groups and electrostatic forces.

Acknowledgment

We acknowledge to CONACyT for financial support through Grant 134111, project CIO-UGTO 2013 and 2014, and scholarship for Andrea Ceja-Fdez. JZZ is grateful to the US NSF for financial support.

References

1. Choi JH, Lee JH, Oh BK, Choi JW (2014) Localized surface plasmon resonance-based label-free biosensor for highly sensitive detection of dopamine. Journal of Nanoscience and Nanotechnology 14:5658-5661.

2. Felton C, Karmakar A, Gartia Y, Ramidi P, Biris AS, Ghosh A (2014) Magnetic nanoparticles as contrast agents in biomedical imaging: Recent advances in iron- and manganese-based magnetic nanoparticles. Drug Metabolism Reviews 46:142-154.

3. Srikar R, Upendran A, Kannan R (2014) Polymeric nanoparticles for molecular imaging. Wiley Interdisciplinary Reviews-Nanomedicine and Nanobiotechnology 6:245-267.

4. Xia XH, Xia YN (2014) Gold nanocages as multifunctional materials for nanomedicine. Frontiers of Physics 9:378-384.

5. Kneipp K, Wang Y, Kneipp H, Perelman LT, Itzkan I, Dasari R, Feld MS (1997) Single molecule detection using surface-enhanced raman scattering (sers). Physical Review Letters 78:1667-1670.

6. Nie SM, Emery SR (1997) Probing single molecules and single nanoparticles by surface-enhanced raman scattering. Science 275:1102-1106.

7. Vlckova B, Pavel I, Sladkova M, Siskova K, Slouf M (2007) Single molecule sers: Perspectives of analytical applications. Journal of Molecular Structure 834:42-47.

8. Li J-F, Ding S-Y, Yang Z-L, Bai M-L, Anema JR, Wang X, Wang A, Wu D-Y, Ren B, Hou S-M, Wandlowski T, Tian Z-Q (2011) Extraordinary enhancement of raman scattering from pyridine on single crystal au and pt electrodes by shell-isolated au nanoparticles. Journal of the American Chemical Society 133:15922-15925.

9. Michaels AM, Nirmal M, Brus LE (1999) Surface enhanced raman spectroscopy of individual rhodamine 6g molecules on large ag nanocrystals. Journal of the American Chemical Society 121:9932-9939.

10. Tian Z-Q, Ren B, Li J-F, Yang Z-L (2007) Expanding generality of surface-enhanced raman spectroscopy with borrowing sers activity strategy. Chemical Communications:3514-3534.

11. Aoki PHB, Furini LN, Alessio P, Aliaga AE, Constantino CJL (2013) Surface-enhanced raman scattering (sers) applied to cancer diagnosis and detection of pesticides, explosives, and drugs. Reviews in Analytical Chemistry 32:55-76.

12. Domenici F, Bizzarri AR, Cannistraro S (2012) Surface-enhanced raman scattering detection of wild-type and mutant p53 proteins at very low concentration in human serum. Analytical Biochemistry 421:9-15.

13. Grubisha DS, Lipert RJ, Park HY, Driskell J, Porter MD (2003) Femtomolar detection of prostate-specific antigen: An immunoassay based on surface-enhanced raman scattering and immunogold labels. Analytical Chemistry 75:5936-5943.

14. Li X, Yang T, Lin J (2012) Spectral analysis of human saliva for detection of lung cancer using surface-enhanced raman spectroscopy. Journal of Biomedical Optics 17.

15. Mohs AM, Mancini MC, Singhal S, Provenzale JM, Leyland-Jones B, Wang MD, Nie S (2010) Hand-held spectroscopic device for in vivo and intraoperative tumor detection: Contrast enhancement, detection sensitivity, and tissue penetration. Analytical Chemistry 82:9058-9065.

16. Sha MY, Xu H, Natan MJ, Cromer R (2008) Surface-enhanced raman scattering tags for rapid and homogeneous detection of circulating tumor cells in the presence of human whole blood. Journal of the American Chemical Society 130:17214-+.

17. Beier HT, Cowan CB, Chou IH, Pallikal J, Henry JE, Benford ME, Jackson JB, Good TA, Cote GL (2007) Application of surface-enhanced raman spectroscopy for detection of beta amyloid using nanoshells. Plasmonics 2:55-64.

18. Choi I, Huh YS, Erickson D (2012) Ultra-sensitive, label-free probing of the conformational characteristics of amyloid beta aggregates with a sers active nanofluidic device. Microfluidics and Nanofluidics 12:663-669.

19. Yao CK, Liao JD, Chang CW, Lin JR (2012) Spatially reinforced nano-cavity array as the sers-active substrate for detecting hepatitis virus core antigen at low concentrations. Sensors and Actuators B-Chemical 174:478-484.

20. An J-H, El-Said WA, Yea C-H, Kim T-H, Choi J-W (2011) Surface-enhanced raman scattering of dopamine on self-assembled gold nanoparticles. Journal of Nanoscience and Nanotechnology 11:4424-4429.

21. Shi C, Zhang Y, Gu C, Seballos L, Zhang JZ (2008) Low concentration biomolecular detection using liquid core photonic crystal fiber (lcpcf) sers sensor - art. No. 685204. In: Gannot I (ed) Optical fibers and sensors for medical diagnostics and treatment applications viii, vol 6852. Proceedings of the society of photo-optical instrumentation engineers (spie). pp 85204-85204. doi:10.1117/12.760117

22. Stiles PL, Dieringer JA, Shah NC, Van Duyne RR (2008) Surface-enhanced raman spectroscopy. In: Annual review of analytical chemistry, vol 1. Annual review of analytical chemistry. pp 601-626. doi:10.1146/annurev.anchem.1.031207.112814

23. Jensen L, Aikens CM, Schatz GC (2008) Electronic structure methods for studying surface-enhanced raman scattering. Chemical Society Reviews 37:1061-1073.

24. Atwater ABaHA (2011) Low-loss plasmonic metamaterials Science 21:290-291.

25. Kosuda KB, JM; Wustholz, KL; Van Duyne, RP. (2011) Nanostructures and surface-enhanced raman spectroscopy. In: Andrews DL S, GD and Wiederrecht GP (ed) Comprehensive nanoscience and technology, vol 3 Oxford: Academic Press, pp 263-301

26. Van Duyne RP, Hulteen JC, Treichel DA (1993) Atomic-force microscopy and surface-enhanced raman-spectroscopy ag island films and ag film over polymer nanosphere surfaces supported on glass. Journal of Chemical Physics 99:2101-2115.

27. Perassi EM, Hernandez-Garrido JC, Moreno MS, Encina ER, Coronado EA, Midgley PA (2010) Using highly accurate 3d nanometrology to model the optical properties of highly irregular nanoparticles: A powerful tool for rational design of plasmonic devices. Nano Letters 10:2097-2104.

28. Sharma Y, Dhawan A (2014) Hybrid nanoparticle-nanoline plasmonic cavities as sers substrates with gap-controlled enhancements and resonances. Nanotechnology 25.

29. Preciado-Flores S, Wang D, Wheeler DA, Newhouse R, Hensel JK, Schwartzberg A, Wang L, Zhu J, Barboza-Flores M, Zhang JZ (2011) Highly reproducible synthesis of hollow gold nanospheres with near infrared surface plasmon absorption using pvp as stabilizing agent. Journal of Materials Chemistry 21:2344-2350.

30. Schwartzberg AM, Olson TY, Talley CE, Zhang JZ (2006) Synthesis, characterization, and tunable optical properties of hollow gold nanospheres. Journal of Physical Chemistry B 110:19935-19944.

31. Wheeler DA, Newhouse RJ, Wang H, Zou S, Zhang JZ (2010) Optical properties and persistent spectral hole burning of near infrared-absorbing hollow gold nanospheres. Journal of Physical Chemistry C 114:18126-18133.

32. Xu S, Hartvickson S, Zhao JX (2008) Engineering of sio(2)-au-sio(2) sandwich nanoaggregates using a building block: Single, double, and triple cores for enhancement of near infrared fluorescence. Langmuir 24:7492-7499.

33. Atkinson RL, Zhang M, Diagaradjane P, Peddibhotla S, Contreras A, Hilsenbeck SG, Woodward WA, Krishnan S, Chang JC, Rosen JM (2010) Thermal enhancement with optically activated gold nanoshells sensitizes breast cancer stem cells to radiation therapy. Science Translational Medicine 2.

34. Barbosa S, Agrawal A, Rodriguez-Lorenzo L, Pastoriza-Santos I, Alvarez-Puebla RA, Kornowski A, Weller H, Liz-Marzan LM (2010) Tuning size and sensing properties in colloidal gold nanostars. Langmuir 26:14943-14950.

35. Huang X, Neretina S, El-Sayed MA (2009) Gold nanorods: From synthesis and properties to biological and biomedical applications. Advanced Materials 21:4880-4910.

36. Trigari S, Rindi A, Margheri G, Sottini S, Dellepiane G, Giorgetti E (2011) Synthesis and modelling of gold nanostars with tunable morphology and extinction spectrum. Journal of Materials Chemistry 21:6531-6540.

37. Xia Y, Li W, Cobley CM, Chen J, Xia X, Zhang Q, Yang M, Cho EC, Brown PK (2011) Gold nanocages: From synthesis to theranostic applications. Accounts of Chemical Research 44:914-924.

38. Zhang JZ (2010) Biomedical applications of shape-controlled plasmonic nanostructures: A case study of hollow gold nanospheres for photothermal ablation therapy of cancer. Journal of Physical Chemistry Letters 1:686-695.

39. Jain PK, Lee KS, El-Sayed IH, El-Sayed MA (2006) Calculated absorption and scattering properties of gold nanoparticles of different size, shape, and composition: Applications in biological imaging and biomedicine (- 2006/03/18). Physical Chemistry - 110:- 7248.

40. Chen Q, Wang C, Cheng L, He WW, Cheng Z, Liu Z (2014) Protein modified upconversion nanoparticles for imaging-guided combined photothermal and photodynamic therapy. Biomaterials 35:2915-2923.

41. Strong LE, Dahotre SN, West JL (2014) Hydrogel-nanoparticle composites for optically modulated cancer therapeutic delivery. Journal of Controlled Release 178:63-68.

42. Wang X, Li YJ, Song ZG, Yin ZY, Qiu JB, Yang ZW, Zhou DC, Yang Y, Zhao ZY, Li C, Yang N, Wang Q (2014) Alpha-nayf4:Nd3+ nanocrystal with near-infrared to near-infrared luminescence for bioimaging applications. Journal of Nanoscience and Nanotechnology 14:3910-3913.

43. Burda C, Chen XB, Narayanan R, El-Sayed MA (2005) Chemistry and properties of nanocrystals of different shapes. Chemical Reviews 105:1025-1102.

44. Lal S, Link S, Halas NJ (2007) Nano-optics from sensing to waveguiding. Nature Photonics 1:641-648.

45. Sau TK, Rogach AL, Jackel F, Klar TA, Feldmann J (2010) Properties and applications of colloidal nonspherical noble metal nanoparticles. Advanced Materials 22:1805-1825.

46. Vo-Dinh T, Dhawan A, Norton SJ, Khoury CG, Wang H-N, Misra V, Gerhold MD (2010) Plasmonic nanoparticles and nanowires: Design, fabrication and application in sensing. Journal of Physical Chemistry C 114:7480-7488.

47. Handley DA (1989) Colloidal gold: Principles, methods and applications. In, vol 1. Academic Press, San Diego, CA.,

48. Henglein A (1999) Radiolytic preparation of ultrafine colloidal gold particles in aqueous solution: Optical spectrum, controlled growth, and some chemical reactions. Langmuir 15:6738-6744.

49. Turkevich J, Garton G, Stevenson PC (1954) The color of colloidal gold. Journal of Colloid Science - 9, Supplement 1:- 35.

50. Brust M, Walker M, Bethell D, Schiffrin DJ, Whyman R (1994) Synthesis of thiol-derivatized gold nanoparticles in a 2-phase liquid-liquid system. Journal of the Chemical Society-Chemical Communications:801-802.

51. Selvakannan PR, Mandal S, Pasricha R, Adyanthaya SD, Sastry M (2002) One-step synthesis of hydrophobized gold nanoparticles of controllable size by the reduction of

aqueous chloroaurate ions by hexadecylaniline at the liquid-liquid interface. Chemical Communications:1334-1335.

52. Tian Y, Hue R, Yu J, Chen B, Sun J, Cheng L (2010) Silica-coated caf2:Eu3+ nanoparticles functionalized with oxalic acid for bio-conjugation to bsa proteins. Chinese Journal of Chemistry 28:921-927.

53. Wolcott A, Gerion D, Visconte M, Sun J, Schwartzberg A, Chen SW, Zhang JZ (2006) Silica-coated cdte quantum dots functionalized with thiols for bioconjugation to igg proteins. Journal of Physical Chemistry B 110:5779-5789.

54. Parakhonskiy BV, Svenskaya YI, Yashchenok AM, Fattah HA, Inozemtseva OA, Tessarolo F, Antolini R, Gorin DA (2014) Size controlled hydroxyapatite and calcium carbonate particles: Synthesis and their application as templates for sers platform. Colloids and Surfaces B-Biointerfaces 118:243-248.

55. Jung GB, Bae YM, Lee YJ, Ryu SH, Park HK (2013) Nanoplasmonic au nanodot arrays as an sers substrate for biomedical applications. Applied Surface Science 282:161-164.

56. Kong KV, Ho CJH, Gong T, Lau WKO, Olivo M (2014) Sensitive sers glucose sensing in biological media using alkyne functionalized boronic acid on planar substrates. Biosensors & Bioelectronics 56:186-191.

57. Kong KV, Lam Z, Lau WKO, Leong WK, Oivo M (2013) A transition metal carbonyl probe for use in a highly specific and sensitive sers-based assay for glucose. Journal of the American Chemical Society 135:18028-18031.

58. Sun F, Bai T, Zhang L, Ella-Menye J-R, Liu S, Nowinski AK, Jiang S, Yu Q (2014) Sensitive and fast detection of fructose in complex media via symmetry breaking and signal amplification using surface-enhanced raman spectroscopy. Analytical Chemistry 86:2387-2394.

59. Tran Thi Bich Q, Su W-N, Chen K-J, Pan C-J, Rick J, Chang C-C, Hwang B-J (2013) Au@sio2 core/shell nanoparticle assemblage used for highly sensitive sers-based determination of glucose and uric acid. Journal of Raman Spectroscopy 44:1671-1677.

60. Camden JP, Dieringer JA, Zhao J, Van Duyne RP (2008) Controlled plasmonic nanostructures for surface-enhanced spectroscopy and sensing. Accounts of Chemical Research 41:1653-1661.

61. Yuen JM, Shah NC, Walsh JT, Glucksberg MR, Van Duyne RP (2010) Transcutaneous glucose sensing by surface-enhanced spatially offset raman spectroscopy in a rat model. Analytical Chemistry 82:8382-8385.

62. Zhang X, Shah NC, Van Duyne RP (2006) Sensitive and selective chem/biosensing based on surface-enhanced raman spectroscopy (sers). Vibrational Spectroscopy 42:2-8.

63. Yang X, Zhang AY, Wheeler DA, Bond TC, Gu C, Li Y (2012) Direct molecule-specific glucose detection by raman spectroscopy based on photonic crystal fiber. Analytical and Bioanalytical Chemistry 402:687-691.

64. Dinish US, Yaw FC, Agarwal A, Olivo M (2011) Development of highly reproducible nanogap sers substrates: Comparative performance analysis and its application for glucose sensing. Biosensors & Bioelectronics 26:1987-1992.

65. Al-Ogaidi I, Gou H, Al-Kazaz AKA, Aguilar ZP, Melconian AK, Zheng P, Wu N (2014) A gold@silica core-shell nanoparticle-based surface-enhanced raman scattering biosensor for label-free glucose detection. Analytica Chimica Acta 811:76-80.

66. Yuan H, Khoury CG, Hwang H, Wilson CM, Grant GA, Tuan V-D (2012) Gold nanostars: Surfactant-free synthesis, 3d modelling, and two-photon photoluminescence imaging. Nanotechnology 23.

67. Ahmed W, Kooij ES, van Silfhout A, Poelsema B (2010) Controlling the morphology of multi-branched gold nanoparticles. Nanotechnology 21.

68. Kawamura G, Yang Y, Fukuda K, Nogami M (2009) Shape control synthesis of multi-branched gold nanoparticles. Materials Chemistry and Physics 115:229-234.

69. Liu MZ, Guyot-Sionnest P (2005) Mechanism of silver(i)-assisted growth of gold nanorods and bipyramids. Journal of Physical Chemistry B 109:22192-22200.

70. Orendorff CJ, Murphy CJ (2006) Quantitation of metal content in the silver-assisted growth of gold nanorods. Journal of Physical Chemistry B 110:3990-3994.

71. N. C. Shah JMY, O. Lyandres, M. R. Glucksberg, J. T. Walsh and R.P. Van Duyne (2010) Surface-enhanced raman spectroscopy for glucose sensing. In: Stenken JA, Cunningham, D. E., Eds. (ed) In vivo glucose sensing, vol 174. A series of monographs on analytical chemistry and its applications. John Wiley & Sons, Inc., pp 421-443

72. Kimling J, Maier M, Okenve B, Kotaidis V, Ballot H, Plech A (2006) Turkevich method for gold nanoparticle synthesis revisited (- 2006/07/21). - 110:- 15707.

73. Yuan H, Ma W, Chen C, Zhao J, Liu J, Zhu H, Gao X (2007) Shape and spr evolution of thorny gold nanoparticles promoted by silver ions. Chemistry of Materials 19:1592-1600.

74. Liz-Marzan LM (2006) Tailoring surface plasmons through the morphology and assembly of metal nanoparticles. Langmuir 22:32-41.

75. Perez-Juste J, Pastoriza-Santos I, Liz-Marzan LM, Mulvaney P (2005) Gold nanorods: Synthesis, characterization and applications. Coordination Chemistry Reviews 249:1870-1901.

76. Mie G (1908) Articles on the optical characteristics of turbid tubes, especially colloidal metal solutions. Annalen Der Physik 25 377-445.

77. Gans R (1912) The shape of ultra microscopic gold particles. Annalen Der Physik 37:881-900.

78. Kobayashi Y, Correa-Duarte MA, Liz-Marzan LM (2001) Sol-gel processing of silica-coated gold nanoparticles. Langmuir 17:6375-6379.

79. Hunt JD, Kavner A, Schauble EA, Snyder D, Manning CE (2011) Polymerization of aqueous silica in h(2)o-k2o solutions at 25-200 degrees c and 1 bar to 20 kbar. Chemical Geology 283:161-170.

80. Kumar PS, Pastoriza-Santos I, Rodriguez-Gonzalez B, Garcia de Abajo FJ, Liz-Marzan LM (2008) High-yield synthesis and optical response of gold nanostars. Nanotechnology 19:6.

81. Jiang J, Bosnick K, Maillard M, Brus L (2003) Single molecule raman spectroscopy at the junctions of large ag nanocrystals. Journal of Physical Chemistry B 107:9964-9972.

82. Kelly KL, Coronado E, Zhao LL, Schatz GC (2003) The optical properties of metal nanoparticles: The influence of size, shape, and dielectric environment. Journal of Physical Chemistry B 107:668-677.

83. Gao XQ, He J, Deng L, Cao HN (2009) Synthesis and characterization of functionalized rhodamine b-doped silica nanoparticles. Optical Materials 31:1715-1719.

84. Wheeler DA, Adams SA, Lopez-Luke T, Torres-Castro A, Zhang JZ (2012) Magnetic fe3o4-au core-shell nanostructures for surface enhanced raman scattering. Annalen Der Physik 524:670-679.

85. López-Luke T, Wheeler DA, De la Rosa E, Torres-Castro A, Adams SA, Zavodivker LS, Zhang JZ (2012) Synthesis, characterization and surface enhanced raman scattering of hollow gold–silica double shell nanostructures. Biomedical Spectroscopy and Imaging 01:275-291.

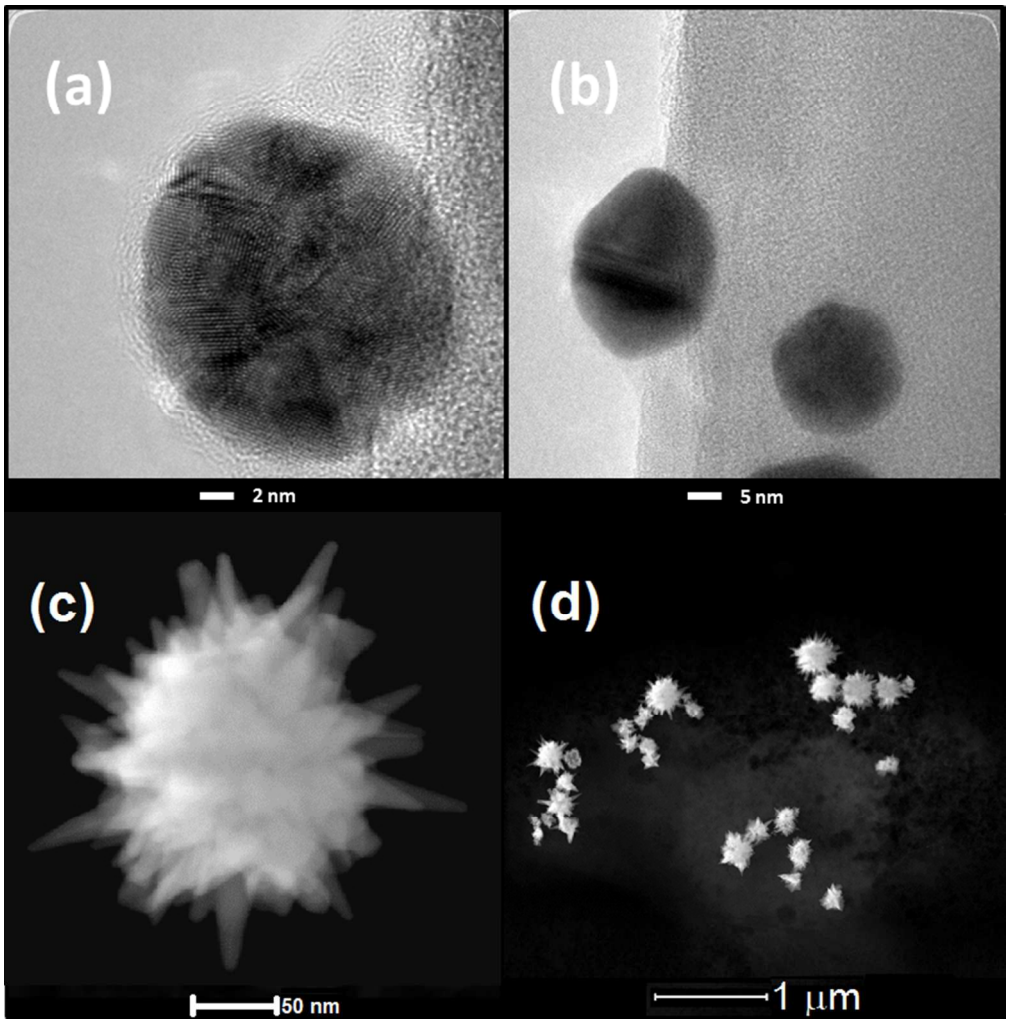

TEM image of AuNPs (a and b) with average size of ~20 nm, which were used to prepare MBGNs (c) with average diameter 200 nm. Aggregates of MBGNs-silica (d) resulting in an average size of 1000 nm
141x143mm (144 x 144 DPI)

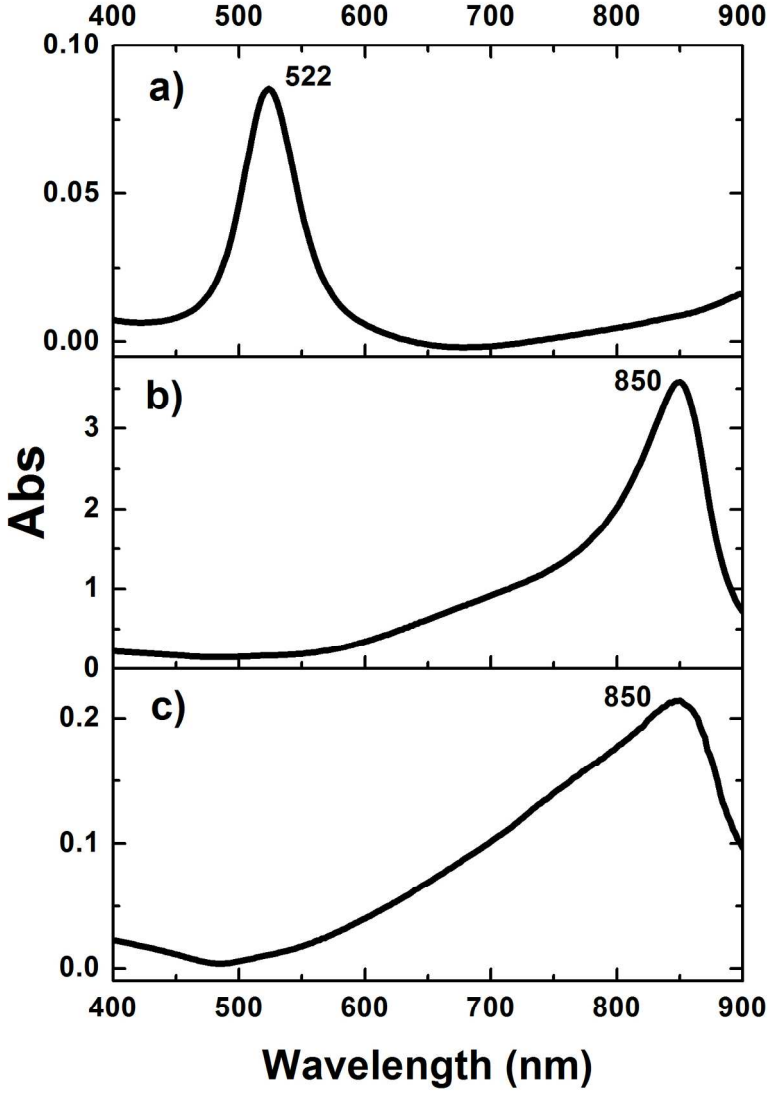

UV-Vis absorption spectra of (a) AuNPs, (b) MBGNs and (c) MBGNs-silica, dispersed in aqueous solution
289x414mm (150 x 150 DPI)

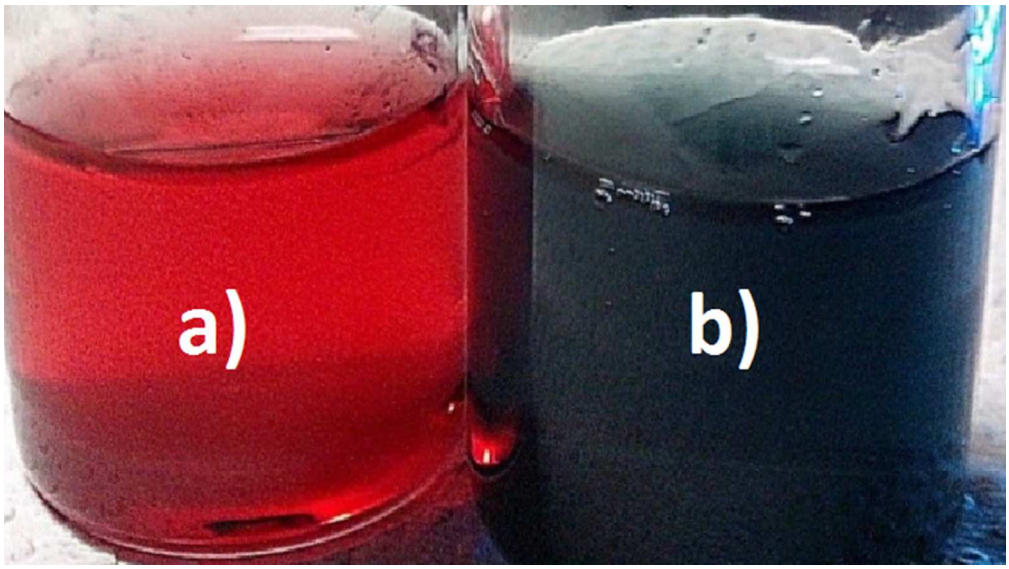

Color Comparison of the solutions. (a) AuNPs (red solution), used as a seed for the synthesis of (b) MBGNs-silica (green-black)
187x104mm (96 x 96 DPI)

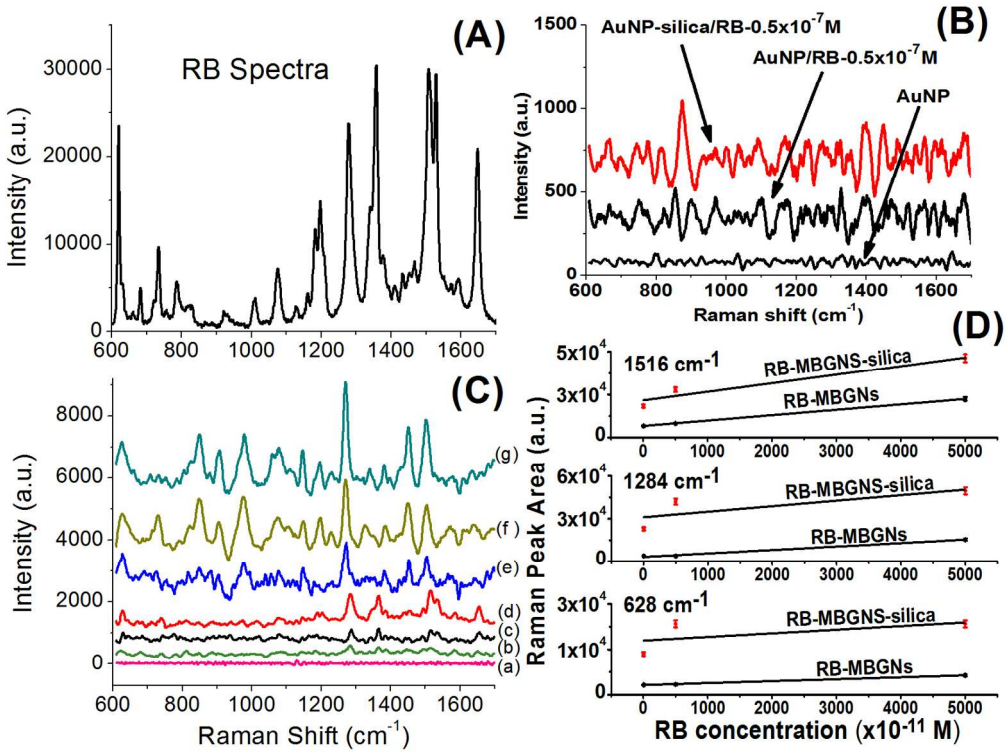

(A) Raman spectra obtained from a concentrated solution (0.01 M) of Rhodamine B in distilled water. (B) Raman signal of AuNP 0M and AuNP and AuNP-silica with RB solution at 1x10-7 M. (C) Representative SERS spectra following 785 nm excitation obtained from: (a) Target MBGNs-silica, and RB at different concentration, 0.5x10-10, x10-8 and x10-7 M on MBGNs (b), (c) and (d), and (e-g) for silica coated MBGNs. (D) A plot of the integrated Raman signal for three peaks, (628, 1284 and 1516 cm-1) vs. the RB concentration as RB on MBGNs (RB/MBGNs) and RB-APTES solution on MBGNs-silica (RB/MBGNs-silica). Each point represents the average value from three SERS spectra and error bars show the standard deviations

289x221mm (150 x 150 DPI)

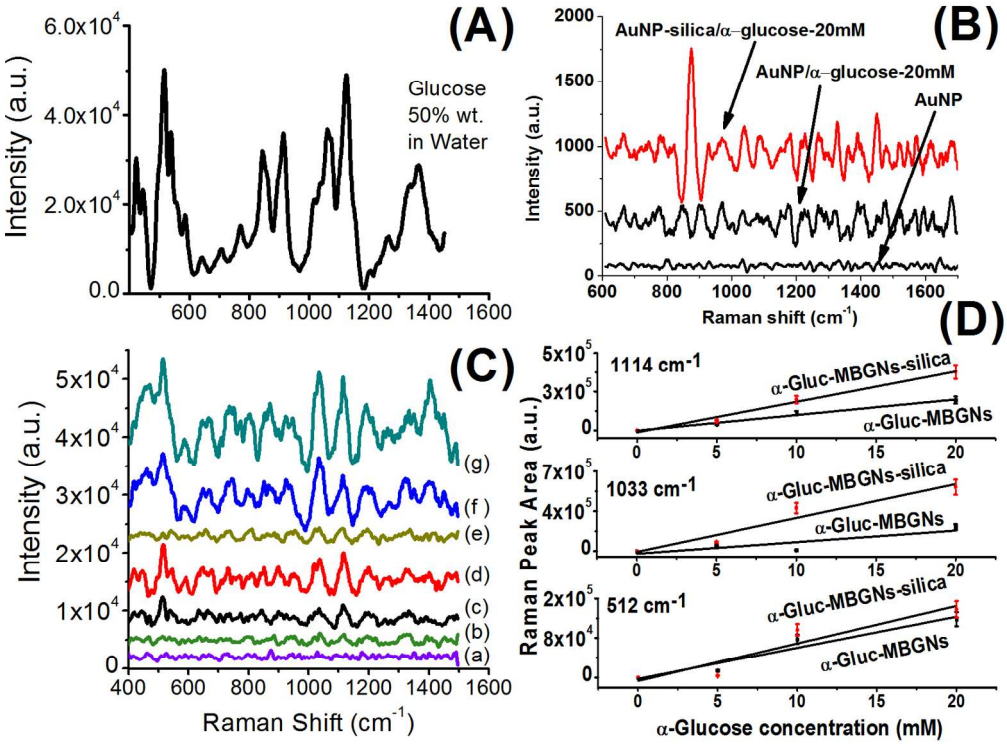

(A) Raman spectra obtained from a concentrated solution of α-glucose in distilled water (50% wt.). (B) Raman signal of AuNP 0M and AuNPs and AuNP-silica with α-glucose in water at 20 mM, (C) Representative SERS spectra following 785 nm excitation obtained from: (a) Target MBGNs-silica, and α-glucose at different concentrations (5, 10 and 20 mM) on MBGNs (b-d), and (e-g) for silica coated MBGNs. In this last case, α-glucose was functionalized with APTES. (D) A plot of the integrated Raman signal (512, 1033 and 1114 cm-1) vs. α-glucose concentration as α-glucose on MBGNs (α-glucose/MBGNs) and α-glucose/APTES solution on MBGNs-silica (α-glucose/MBGNs-silica). Each point represents the average value from three SERS spectra and error bars show the standard deviations
289x221mm (150 x 150 DPI)

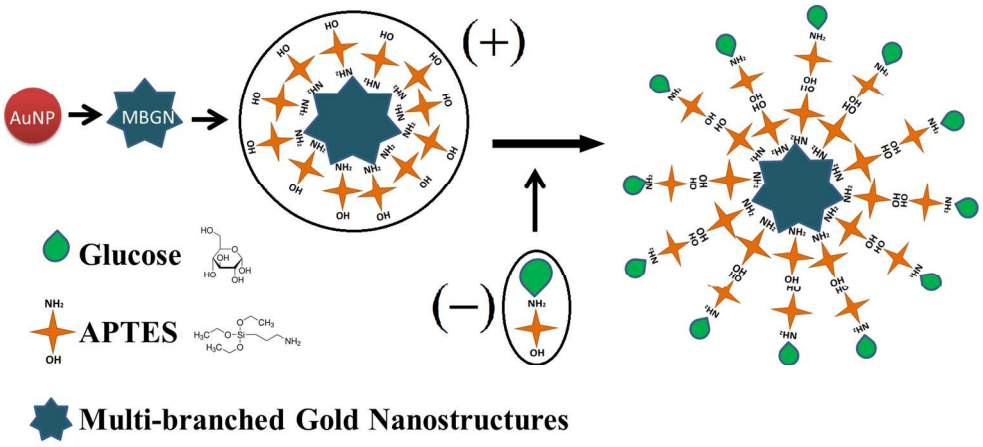

Schematic diagram showing hypothetical addition of α-glucose to MBGNs. APTES solution was added to the MBGNs, and α-glucose/APTES solution was prepared and subsequently both solutions were mixed. This facilitated the α-glucose incorporation through the bonds of hydroxyl groups and electrostatic forces
334x150mm (144 x 144 DPI)